Cylindrically symmetric electrohydrodynamic patterning

Paru Deshpande,[1,*] Leonard F. Pease III,[2,†] Lei Chen,[1,‡] Stephen Y. Chou,[1] and William B. Russel[2]

[1]*Department of Electrical Engineering, Princeton University, Princeton, New Jersey 08544, USA*
[2]*Department of Chemical Engineering, Princeton University, Princeton, New Jersey 08544, USA*

Cylindrically symmetric structures such as concentric rings and rosettes arise out of thin polymeric films subjected to strong electric fields. Experiments that formed concentric rings and theory capable of explaining these and other cylindrical structures are presented. These rings represent an additional member of a class of structures, including pillars and holes, formed by electrohydrodynamic patterning of thin films, occasionally referred to as lithographically induced self-assembly. Fabrication of a set of concentric rings begins by spin coating a thin poly(methyl methacrylate) film onto a silicon wafer. A mask is superimposed parallel to the film leaving a similarly thin air gap. Electric fields, acting in opposition to surface tension, destabilize the free interface when raised above the glass transition temperature. Central pillars nucleate under small cylindrical protrusions patterned on the mask. Rings then emerge sequentially, with larger systems having as many as 10 fully formed rings. Ring-to-ring spacings and annular widths, typically on the order of a micron, are approximately constant within a concentric cluster. The formation rate is proportional to the viscosity and, consequently, has the expected Williams-Landel-Ferry dependence on temperature. In light of these developments we have undertaken a linear stability analysis in cylindrical coordinates to describe these rings and ringlike structures. The salient feature of this analysis is the use of perturbations that incorporate their radial dependence in terms of Bessel functions as opposed to the traditional sinusoids of Cartesian coordinates. The theory predicts approximately constant ring-to-ring spacings, constant annular widths, and growth rates that agree with experiment. A secondary instability is observed at higher temperatures, which causes the rings to segment into arcs or pillar arrays. The cylindrical theory may be generalized to describe hexagonal pillar/hole packing, gratings, and rosettes with the first being of particular importance given the ubiquitous observation of hexagonal packing. The perturbation analysis presented here is relevant to any system with cylindrical symmetry, for which the radial dependence can be described in terms of Bessel functions.

I. INTRODUCTION

Patterning thin organic films has become an issue of great technical importance. The semiconductor industry routinely relies on photolithography of polymer resist films to delineate devices and interconnects; however, the chemicals and radiation exposures used in photolithography are unsuitable for many applications and scaling down the feature size requires scaling up the cost. As such, alternative patterning processes being pursued include nanoimprint lithography [1], microcontact printing [2], and cold-welding [3]. Patterns that form spontaneously or in response to electric fields may eventually provide another class of alternatives. Options currently being pursued include self-assembly of colloidal particles [4] and phase separation of block copolymers [5].

In this paper we discuss another approach, which capitalizes on the growth of instabilities to pattern thin polymer melts. This electrohydrodynamic patterning method, which has been termed lithographically induced self-assembly (LISA), has been shown to produce periodic pillar arrays and mesas [6–8]. Furthermore, the feature size of the resulting patterns can be reduced to the submicron scale [8,9].

In a typical experiment [6], a thin polymer film is first spun onto a flat substrate. A mask, sometimes patterned in relief, is held in close proximity to the polymer surface, leaving an air gap, and the system is heated above the glass transition temperature, T_g, of the polymer (Fig. 1). In some cases an external electric field is applied though this is not always necessary. An instability then causes perturbations at the polymer surface to grow with a length scale set by the competition between electrical forces and surface tension. After some time the polymer film is observed to assemble into periodic structures that bridge the gap between the mask and substrate. By using a patterned mask, the location and domain orientation of the structures can be well controlled. Single domain pillar arrays can be formed with appropriate relief dimensions. After cooling the system below the polymer T_g, the structures become fixed and the mask can be removed.

Models to predict the spacings agree on the electrohydrodynamic nature of the process, but differ regarding the electrical properties of the film. While Chou and Zhuang [6] initially proposed that image charge generated the electrical forces, Schäffer *et al.* [8,10] affirmed electrical forces to be the main driving force by observing spacings that vary inversely with the electric field as predicted by their model. They assumed the film to be absent of free charge, i.e., a perfect dielectric, and identified the linearly unstable modes within the context of the lubrication approximation as set by the competition between the electrical forces and the surface

*Email address: pad@princeton.edu
†Email address: lpease@princeton.edu
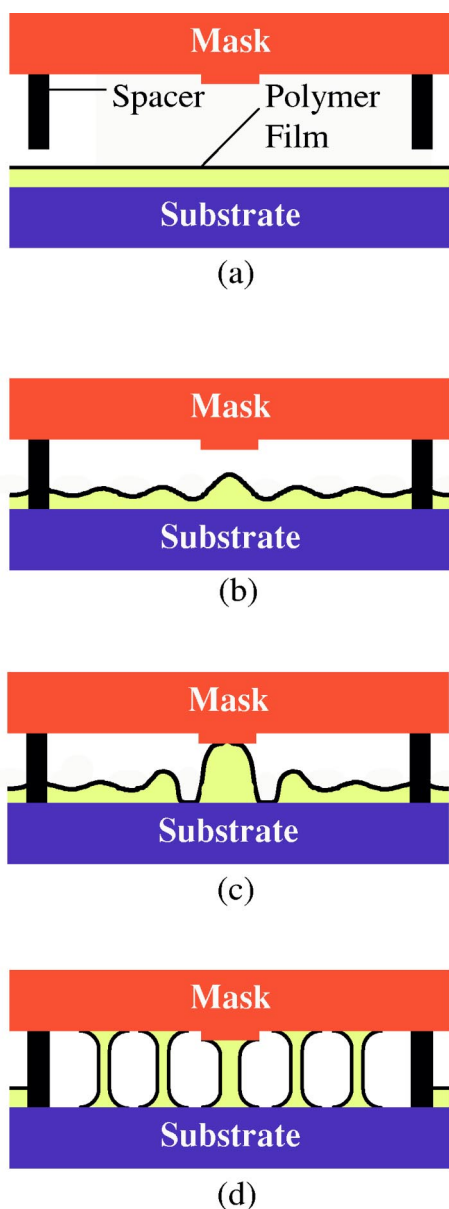‡Present address: NanoOpto Corp., Somerset, NJ 08873, USA.

FIG. 1. (Color online) Schematic of ring formation by electro-hydrodynamic patterning. (a) A mask patterned with localized protrusions is held above a thin polymer film. Spacers on the mask ensure that the mask protrusion does not initially contact the polymer surface. (b) The system is placed in a press and heated above the glass transition temperature of the polymer. A cylindrically symmetric instability sets in driven by electric fields and opposed by surface tension. (c) A central pillar forms beneath the protrusion after which (d) concentric rings are observed to form sequentially around the pillar.

tension. They justified the linear stability analysis by demonstrating that the spacings agree with the fastest growing wave numbers predicted. Lin *et al.* [11] adapted their model to account for a dielectric medium in the gap by including its viscosity and dielectric constant also under the framework of the lubrication approximation. Zhuang [12], in a similar linear stability analysis, included the effect of static charge

imposed at the surface of the film in the expression for the normal stress balance; his results reduce to Schäffer's when the static charge is negligible. By including the effect of free charge in the polymer film, Pease and Russel [13] developed the leaky dielectric model, which allows for redistribution of charges at the interfaces. Results of the linear stability analysis showed that the leaky dielectric yields growth exponents and characteristic wave numbers larger than that for the perfect dielectric. Pease and Russel [14] also contrasted the results of the linear stability analysis with and without the lubrication approximation, thus showing that this approximation fails where surface tension is small and electric fields are large. Relaxation of the approximation predicts more tightly packed pillars with greater aspect ratios. Comparison of the theory developed for pattern-free masks shows reasonable agreement with data for pillar and hole arrays from the literature [15].

While the fundamentals of this patterning process under pattern-free masks are reasonably well understood, recent cylindrically symmetric structures challenge the existing theory. The literature contains several examples of these structures. Chou [16] detailed two examples of concentric rings with four to five rings each surrounding a central pillar. The rings were evenly spaced and the annular widths of the rings appeared to be constant. Schäffer *et al.* [8] have shown a rosette in which 12 pillars circumscribe a central pillar. They implicated a locally accentuated electric field as the cause of the rosette's formation. Subsequent work in their group [17] has indicated that competition between electrohydrodynamic flow and dewetting may play a role in their rosette features. Zhuang observed rings of pillars surrounding spacers and dust particles [12] and also spirals and gratings in cases with pattern-free masks and low-energy substrates. These observations present interesting challenges to existing theories.

In this paper we examine the experiments and experimental conditions that give rise to some of the ringlike features. These results are compared to an electrohydrodynamic model of the process capable of describing these cylindrical structures. The perturbation analysis contained herein has relevance to other cylindrically symmetric systems for which Bessel functions also capture the radial variation.

II. EXPERIMENT

The experimental procedure is summarized schematically in Fig. 1 and is similar to that used in previous experiments [6]. The poly(methyl methacrylate) (PMMA) with a molecular weight of $M_w = 2$ kg/mol (Polymer Source) used in these experiments has a polydispersity index of 1.07. The polymer was combined with an aliphatic quaternary amine (5% of PMMA weight), octadecyl poly (15) oxyethylene methyl ammonium chloride (Tomah Products, Product No. Q-18-15), and dissolved in chlorobenzene (1–2 % solution by weight of polymer). The quaternary ammonium chloride was selected for its solubility in PMMA. The solution was spin

coated to a thickness of 90 nm on a polished silicon wafer.[1] The glass transition temperature of our polymer system was measured by differential scanning calorimetry to be 75 °C.

Two different mask materials were used in our experiment: fused quartz and silicon with a 130 nm layer of thermally grown oxide. In both cases the mask was patterned with protrusions ranging in height from 10 to 40 nm using photolithography followed by reactive ion etching (RIE) in a CHF_3 plasma. Each protrusion was cylindrical with a diameter of 3 μm. The protrusions, which do not initially contact the polymer surface, act as a nucleation points for ring development. Nonuniformities in the polymer film or mask surface can also nucleate rings indicating that the protrusions are not necessary but may be helpful in locating the centers of sets of rings. The gap between the mask and polymer surfaces is controlled by an array of spacers fabricated on the mask surface in the form of 0.5 mm wide aluminum lines separated by 5 mm. The aluminum was deposited by electron beam evaporation through a shadow mask to create spacers with heights ranging from 140 to 190 nm. It should be noted that some of the heights of rings reported in the plots are larger than the spacers on any of the masks used in our experiment. It may be that the spacers were not forced to the bottom of the polymer film, were not locally in contact with the polymer surface perhaps due to dust particles, or the rings may have been stretched during removal of the mask. Finally, the masks are coated with a low surface energy surfactant, a fluorinated alkyltrichlorosilane, to facilitate the separation of the mask from the polymer after the rings have formed.

The mask is held against the polymer surface by a parallel-plate press with an applied pressure of 300 psi (21 MPa). Such pressures minimize variation in the gap between the mask and polymer surfaces. The entire system is heated above the glass transition temperature of the film to initiate the assembly process. After a specified time the system is cooled below the glass transition temperature to affix the patterns, and the mask is removed. There is no externally applied field in our experiments. The polymer surface is then characterized using atomic force and optical microscopy.

Figure 2 shows an atomic force microscopy (AFM) image of completed concentric rings in which the central pillar is clearly visible. The annular width of the rings is 1 μm and the ring-to-ring spacing is 3 μm. The rings are 170 nm high (as measured from the substrate to the top of the ring) and took 60 min to form at 95 °C. Up to 10 fully formed rings have been seen around a single central pillar. More rings form as the dwell time increases.

Figure 3 shows an array of single rings formed under a mask with 40 nm high protrusions spaced 40 μm apart. The rings took 30 min to form at 90 °C. Each set of rings centers on a protrusion patterned in relief on the mask, but does not
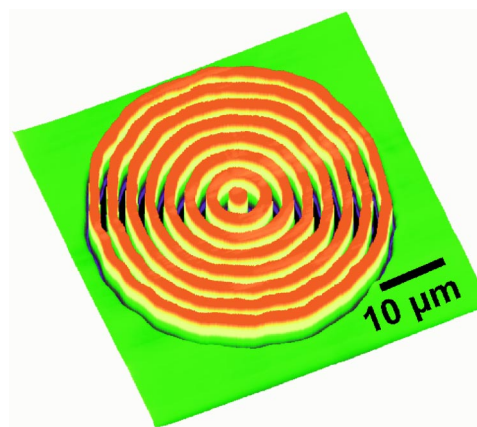

FIG. 2. (Color online) Atomic force microscopy image of typical ring pattern formed from a 90 nm PMMA film containing 5% quaternary ammonium chloride. The rings are 170 nm tall and have a linewidth of 1 μm with a radial spacing of 3 μm. The mask and substrate are made of silicon and the former has 130 nm of thermally grown oxide. The sidewalls are quite steep and the tops of the rings are flat.

show the central pillar that would be expected beneath the mask protrusion. The reason is simple: the polymer tends to climb the sidewalls of the protrusion and is torn away when the mask is removed. This problem is not observed with the smaller 10 nm protrusions. With protrusions of this height, however, nucleation in unwanted areas is more likely to occur, often at localized nonuniformities in the mask or polymer film. Experiments were also performed to observe directly the kinetics of ring formation. The experimental setup resembles that discussed previously but necessitates the use of a quartz mask. The formation process was recorded through the top of the mask with optical microscopy. Further details of the setup can be found elsewhere [18]. These observations and comparison to our theoretical model will be presented later in this article.

It is important to note the differences between the experimental conditions that form ring structures and those that
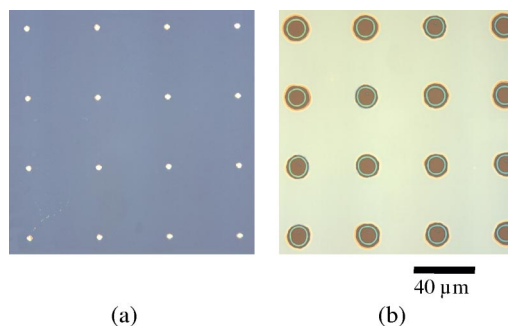

(a)   (b)

FIG. 3. (Color online) Optical micrographs comparing mask and polymer film after LISA process. The silicon mask and substrate appear dark. (a) Optical image of silicon oxide protrusions 40 nm high and 3 μm in diameter on silicon mask. (b) Self-assembled ring patterns formed from a 90 nm film at 90 °C with 160 nm spacer heights and 130 nm of oxide on the mask. No central pillar can be observed because the polymer film had climbed the sidewalls of the protrusion, and was peeled off during separation.

---

[1] The silicon wafers of p-type (100) with boron doping (10–20 $\Omega \cdot$cm) were first cleaned for 15 min in a bath of DI water, hydrogen peroxide, and ammonium hydroxide (5:1:1) at 80 °C followed by a DI water rinse for 15 min. The wafers had a layer of native oxide ($\sim$20–30 Å), though, in some cases an 80 nm layer of thermal oxide was grown.
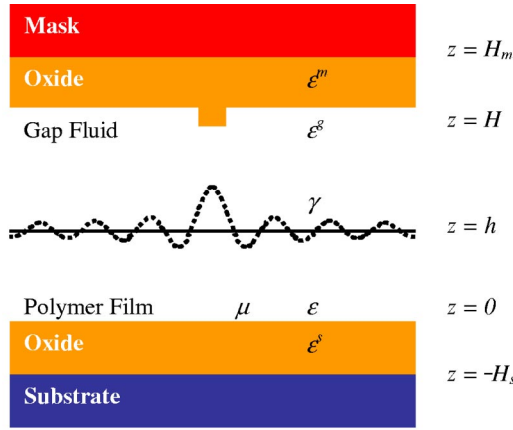
FIG. 4. (Color online) Schematic of the model variables where the height, surface tension, viscosity, and dielectric constant of the polymer film are h, γ, μ, and ε, respectively, while the dielectric constant of the gap fluid is ε^g and the mask–substrate separation is H. Where oxide is present on the mask, ε^m and $H_m - H$ are the dielectric constant and thickness of the oxide, while for the substrate they are ε^s and H_s.

previously created discrete pillars [6]. First, many of the masks were patterned with cylindrical protrusions as in Fig. 3. Second, the quaternary ammonium chloride, a fully soluble species, has been added to the polymer film. Although cylindrically symmetric structures have been observed without this addition, segmentation of the rings is less common with it. This may be a consequence of some secondary instability, which will be addressed later. In addition to differences in film composition, we note that our experiments typically employ smaller mask–substrate separations and lower temperatures than previous work on pillars. At higher temperatures ($\sim 120\ °$C), discrete pillars are once again observed even with the quaternary ammonium chloride (Fig. 12) and cylindrical protrusions on the mask. The model presented below accommodates the most important aspect of these features, namely the cylindrical symmetry.

III. MODELING

Modeling the electrically driven formation of the rings requires a linear stability analysis with a particular form of the perturbation to account for symmetry. The electrohydrodynamic model, which we adopt from Saville [19], is capable of describing fluids ranging from perfect dielectrics, where free charge is absent, to perfect conductors, where the fields in conducting media are suppressed, with so-called "leaky dielectrics" spanning the range in between. For the purposes of this paper we focus on the perfect dielectrics noting that wave numbers and growth exponents for other cases have been developed previously [14] in Cartesian coordinates. We allow electric fields to arise between the mask and substrate either by applying a voltage, V, or through an asymmetry among the contact potentials, χ_i, at the interfaces. Variables are shown in Fig. 4. Our analysis accounts for the reduction of the field in the gap due to oxide layers present on the mask and substrate, which are otherwise assumed to be conductors. The resulting electrical potentials, ψ, give rise

to an electrical surface force at the free interface. Body forces are negligible because there is no gradient in the dielectric constant, ε, and bulk charge is assumed absent. Surface tension, γ, counters the electrical surface force as described in the normal stress balance, Eq. (9). Balancing the two sets the characteristic lateral spacing, L, as described later. The fluid—our film above the glass transition temperature—responds to the resulting lateral pressure gradient, ∇p, with velocity, $\boldsymbol{u} = u_r \boldsymbol{e}_r + u_\theta \boldsymbol{e}_\theta + u_z \boldsymbol{e}_z$, which leads to deformation of the interface at $z = h$ through lateral viscous flow that couples to vertical flow through continuity.

Perturbations in the film height locally accentuate the electric fields, which affect the pressure and hence feed back into the film height through the fluid mechanics. If the electric fields are sufficient to overcome surface tension the free interface becomes unstable. The relevant equations in cylindrical coordinates in SI units, with $\nabla = \boldsymbol{e}_z \partial / \partial z + \boldsymbol{e}_r \partial / \partial r + (\boldsymbol{e}_\theta / r) \partial / \partial \theta$ and $\boldsymbol{e}_z$ as the unit vector in z, are summarized as follows:

$$\nabla^2 \psi^s = 0, \quad \nabla^2 \psi = 0, \quad \nabla^2 \psi^g = 0, \quad \nabla^2 \psi^m = 0, \tag{1}$$

$$\psi^s = V + \chi_0, \quad \text{at } z = -H_s, \tag{2}$$

$$\psi - \psi^s = \chi_1, \quad 0 = \|\varepsilon \varepsilon_o \nabla \psi\| \cdot \boldsymbol{n}, \quad \text{at } z = 0, \tag{3}$$

$$\psi^g - \psi = \chi_2, \quad 0 = \|\varepsilon \varepsilon_o \nabla \psi\| \cdot \boldsymbol{n}, \quad \text{at } z = h, \tag{4}$$

$$\psi^m - \psi^g = \chi_3, \quad 0 = \|\varepsilon \varepsilon_o \nabla \psi\| \cdot \boldsymbol{n}, \quad \text{at } z = H, \tag{5}$$

$$\psi^m = -\chi_4, \quad \text{at } z = H_m, \tag{6}$$

$$-\nabla p + \mu \nabla^2 \boldsymbol{u} = 0, \tag{7}$$

$$\nabla \cdot \boldsymbol{u} = 0, \tag{8}$$

$$\frac{1}{2} \|\varepsilon \varepsilon_o [(\nabla \psi \cdot \boldsymbol{n})^2 - (\nabla \psi \cdot \boldsymbol{t}_r)^2 - (\nabla \psi \cdot \boldsymbol{t}_\theta)^2]\|$$

$$- [-p + \mu \boldsymbol{n} \cdot (\nabla \boldsymbol{u} + \nabla \boldsymbol{u}^t) \cdot \boldsymbol{n}] + \gamma \kappa = 0, \quad \text{at } z = h, \tag{9}$$

$$\mu \boldsymbol{t}_i \cdot (\nabla \boldsymbol{u} + \nabla \boldsymbol{u}^t) \cdot \boldsymbol{n} = 0, \quad \text{at } z = h, \tag{10}$$

$$u_z = 0, \quad u_r = 0, \quad \text{and} \quad u_\theta = 0, \quad \text{at } z = 0, \tag{11}$$

$$\frac{\partial h}{\partial t} = u_z - u_r h_r - \frac{1}{r} u_\theta h_\theta, \quad \text{at } z = h. \tag{12}$$

The first six equations describe the electrostatic potentials (ψ^s, ψ, ψ^g, and ψ^m) in the substrate ($z = -H_s$ to 0), film ($z = 0$ to h), gap ($z = h$ to H), and mask ($z = H$ to H_m), respectively. The latter six equations describing the fluid mechanics couple with the electrostatics through the normal stress balance, Eq. (9). We assume the mask to be grounded, and the jump operator, $\| \ \|$, indicates subtraction of the operand immediately below the interface from that above. The superscript t stands for the transpose.

Equations (1) through (12) are completed with the mean curvature

$$\kappa = \frac{\left(1 + \frac{1}{r^2}h_\theta^2\right)h_{rr} + \frac{2}{r^2}h_r h_\theta\left(\frac{1}{r}h_\theta - h_{r\theta}\right) + (1 + h_r^2)\left(\frac{1}{r}h_r + \frac{1}{r^2}h_{\theta\theta}\right)}{\left(1 + h_r^2 + \frac{1}{r^2}h_\theta^2\right)^{3/2}},$$

(13)

and the normal and tangential unit vectors

$$\boldsymbol{n} = \frac{\boldsymbol{e}_z - h_r\,\boldsymbol{e}_r - \frac{1}{r}h_\theta\boldsymbol{e}_\theta}{\left(1 + h_r^2 + \frac{1}{r^2}h_\theta^2\right)^{1/2}},$$

(14)

$$\boldsymbol{t}_r = \frac{\boldsymbol{e}_r + h_r\boldsymbol{e}_z}{(1 + h_r^2)^{1/2}},$$

(15)

$$\boldsymbol{t}_\theta = \frac{(1 + h_r^2)\boldsymbol{e}_\theta - \frac{1}{r}h_r h_\theta\boldsymbol{e}_r + \frac{1}{r}h_\theta\boldsymbol{e}_z}{(1 + h_r^2)^{1/2}\left(1 + h_r^2 + \frac{1}{r^2}h_\theta^2\right)^{1/2}},$$

(16)

where the subscript to h indicates a partial derivative with respect to this variable and $\boldsymbol{e}_r$, $\boldsymbol{e}_\theta$, and $\boldsymbol{e}_z$ are the unit vectors in the r, θ, and z directions. These equations are solved under the lubrication approximation below with details in the Appendix [20].

The equations were scaled by defining dimensionless variables as given in Table I where the contact potential parameter is $\chi = \chi_0 + \chi_1 + \chi_2 + \chi_3 + \chi_4 + V$ with overbars denoting scaled quantities. The electrocapillary length falls out of the normal stress balance as $L = \sqrt{\gamma H^3/\varepsilon^g\varepsilon_o\chi^2}$, allowing us to construct an important length scale ratio $H/L = \sqrt{\varepsilon^g\varepsilon_o\chi^2/\gamma H}$. The lubrication approximation usually applies when the square of this ratio is much less than unity [14]. This approximation is valid for the experiments reported herein as the fields are relatively small and the surface tension is large. The characteristic process time is $H/U = \mu\gamma H^3/(\varepsilon^g\varepsilon_o\chi^2)^2$. As the viscosity, μ, is strongly temperature dependent, this time scale varies with the usual Williams-Landel-Ferry depen-

TABLE I. Scaling factors.

Variables	Scaled factor
$z, h, H, H_s, H_m, h_{mask}$	H
$r, 1/k$	L
$\psi, \psi^g, \psi^s, \psi^m, \chi_i, V$	χ
p	$\varepsilon^g\varepsilon_o\chi/H^2$
u_z	U
u_r, u_θ	UL/H
t	H/U

dence [21,22]. Additionally, the initial height ratio, $\bar{h}_o = h_o/H$, and the ratio of dielectric constants, $\varepsilon/\varepsilon^g$, generally are important. To first order approximation van der Waals forces are negligible because $AH^2/h^3\varepsilon^g\varepsilon_o\chi^2$ and $AH^2/(H-h)^3\varepsilon^g\varepsilon_o\chi^2$ are much less than unity, where A is Hamaker's constant.

Selection of the appropriate perturbation is the salient difference between the theory developed previously [10,14] and that herein. The previous form of the perturbation was

$$\bar{h} = \bar{h}_o + \tilde{h}\exp(i\bar{\boldsymbol{k}}\cdot\bar{\boldsymbol{x}}_s),$$

(17)

where $\tilde{h}$, the perturbation amplitude, is much smaller than any other length scale, $\bar{\boldsymbol{k}}$ is the wave vector, and $\bar{\boldsymbol{x}}_s$ is a position vector. Equation (17) led to regularly spaced maxima separated by $\lambda = 2\pi L/\bar{k}$ and square packing, despite its frequent application to hexagonal packing. Here, however, we choose a perturbation with the form

$$\bar{h} = \bar{h}_o + \tilde{h}e^{i\nu\theta}J_\nu(\bar{k}\bar{r})$$

(18)

in radial coordinates (r, θ) [23] where $J_\nu(\bar{k}\bar{r})$ is a Bessel function of the first kind of order ν with wave number k. Similar spatial dependencies have been seen in other systems [24,25]. Bessel functions of the second kind, $Y_\nu(\bar{k}\bar{r})$, were not chosen due to their unphysical divergence at $r=0$. Figure 5 shows the zero order $(\nu=0)$ perturbation that yields rings as a function of the argument, $\bar{k}\bar{r}$. Clearly, the maxima, which should correspond approximately to the location of the rings, are not equally spaced for the first couple of rings, but the spacing quickly approaches 2π for subsequent maxima (see Table II). Notably, the spacing of approximately $2\pi L/\bar{k}$ is remarkably similar to that for the pillars/holes [13,14].

We perturb accordingly, noting that the radial velocity has the form $\bar{u}_r = \tilde{u}_r e^{i\nu\theta}dJ_\nu(\bar{k}\bar{r})/d\bar{r}$ and that sums, such as $\bar{h} = \bar{h}_o + \tilde{h}\Sigma_\nu e^{i\nu\theta}J_\nu(\bar{k}\bar{r})$, are allowed in the linear analysis. Steps leading to the determination of the eigenvalue, in the Appendix [20] for the perfect dielectric, parallel previous derivations [13–15] with subtle, though significant, alterations. After substituting the perturbations into the above equations and expanding expressions near the polymer–gap fluid interface $(z=h)$ in a Taylor series expansion, we discard the second- and higher-order terms. Solution for the interfacial height yields a dispersion relation between the growth exponent, $\bar{m}$, which is scaled on the process time scale, H/U, and the wave number, $\bar{k}$, which is scaled on the electrocapillary length, L. These dispersion relations are identical to those
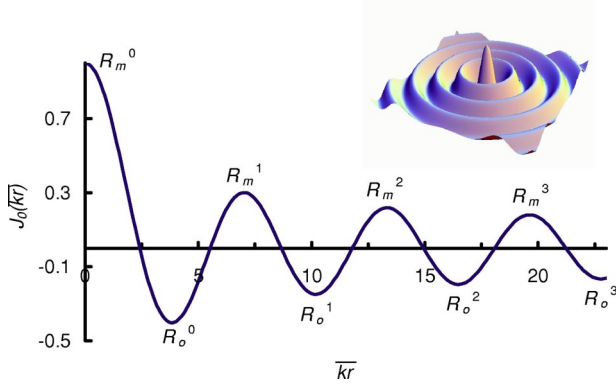
FIG. 5. (Color online) The zeroth order Bessel function as a function of the argument with maxima R_m^n and minima R_o^n. The inset shows the three-dimensional rendition of the perturbation.

developed previously, suggesting that the eigenvalue is more general than the eigenfunction.

If the lubrication approximation is invoked, as is appropriate for the data presented hereafter because the surface tension is large and the potential small, then

$$\bar{m} = \frac{1}{3}\bar{h}_o^3\bar{k}^2\left(\frac{\frac{\varepsilon}{\varepsilon^g}\left(\frac{\varepsilon}{\varepsilon^g}-1\right)^2}{X_D^3} - \bar{k}^2\right), \qquad (19)$$

where the denominator $X_D = \bar{h}_o + (\varepsilon/\varepsilon^g)(1-\bar{h}_o) + (\varepsilon/\varepsilon^m) \times (H_m/H+1) + (\varepsilon/\varepsilon^s)(H_s/H)$ with the first term in the large parentheses arising from the electrical polarization forces and the second from surface tension. The two terms compete with the former dominating for small $\bar{k}$ but yielding to surface tension when $\bar{k}$ is large. This competition determines a maximum growth exponent and wave number, which are

$$\bar{k}_{\max} = \left(\frac{1}{2}\frac{\frac{\varepsilon}{\varepsilon^g}\left(\frac{\varepsilon}{\varepsilon^g}-1\right)^2}{X_D^3}\right)^{1/2}, \qquad (20)$$

TABLE II. Values of the arguments at the *n*th maxima, R_m^n, and minima, R_o^n, of the zeroth order Bessel function of the first kind.

n	R_m^n	R_o^n
0	0	3.83
1	7.02	10.17
2	13.32	16.47
3	19.62	22.76
4	25.90	29.05
5	32.19	35.33
6	38.47	41.62
7	44.76	47.90
8	51.04	54.19
9	57.33	60.47
10	63.61	66.75

$$\bar{m}_{\max} = \frac{1}{3}\bar{h}_o^3\bar{k}_{\max}^4 = \frac{\bar{h}_o^3\dfrac{\varepsilon^2}{\varepsilon^g}\left(\dfrac{\varepsilon}{\varepsilon^g}-1\right)^4}{12X_D^6}. \qquad (21)$$

Both $\bar{k}_{\max}$ and $\bar{m}_{\max}$ are smaller with insulating layers (i.e. oxide layers with thicknesses H_s and $H_m - H$), indicating smaller growth rates and larger spacings. Here we include results only for the perfect dielectric, though both leaky and perfect dielectrics are capable of producing ringlike structures. Once $\bar{k}_{\max}$ is known, the diameter of each ring can be determined.

The measured diameter is the mean of the distance between outer edges of a ring and that between its inner edges,

$$D_n = 2\sqrt{2}R_m^n\left(\frac{\gamma}{\varepsilon_o\chi^2}\frac{\left[\dfrac{h_o}{\varepsilon}+\dfrac{H-h_o}{\varepsilon^g}+\dfrac{H_m-H}{\varepsilon^m}+\dfrac{H_s}{\varepsilon^s}\right]^3}{\left(\dfrac{1}{\varepsilon^g}-\dfrac{1}{\varepsilon}\right)^2}\right)^{1/2}, \qquad (22)$$

for each ring, $n > 0$, where R_m^n is the *n*th scaled maximum of the Bessel function as shown in Fig. 5. As the surface tension, γ, decreases or the electrical potential, symbolized by χ, increases the measured diameter should decrease so long as the lubrication approximation holds [14]. For the first ring or two a correction is developed in the appendicial documentation [20] as more material accumulates from the outer part of the ring than the inner part and the spacing between scaled maxima no longer approximates 2π.

The annular widths may also be determined through a straightforward mass balance based on the Bessel function. We assume that in addition to the maxima of the Bessel function determining the location of the ring, that the sidewalls are exactly flat and not curved due to contact angles with the mask and substrate, and that the fluid is incompressible. Curvature of the sidewalls has been observed [12] and may increase, marginally, the perceived annular width since larger diameters at either the top or the bottom of the ring may be measured. The resulting mass balance predicts that the width of ring n is

$$W_n = 2\sqrt{2}\pi\frac{h_o}{H}\left(\frac{\gamma}{\varepsilon_o\chi^2}\frac{\left[\dfrac{h_o}{\varepsilon}+\dfrac{H-h_o}{\varepsilon^g}+\dfrac{H_m-H}{\varepsilon^m}+\dfrac{H_s}{\varepsilon^s}\right]^3}{\left(\dfrac{1}{\varepsilon^g}-\dfrac{1}{\varepsilon}\right)^2}\right)^{1/2}. \qquad (23)$$

Equation (23) is not a function of R_m^n so it should be independent of the ring number; a correction for the first couple of rings is provided in the appendicial material [20]. This expression points to the importance of the ratio between the initial film thickness and the mask–substrate separation, suggesting that relatively thinner films will generally produce smaller annular widths. Decreasing the surface tension or increasing the driving potential also minimizes the annular width. One ring is not expected to merge with another in the same set regardless of the relative thickness of the film, in
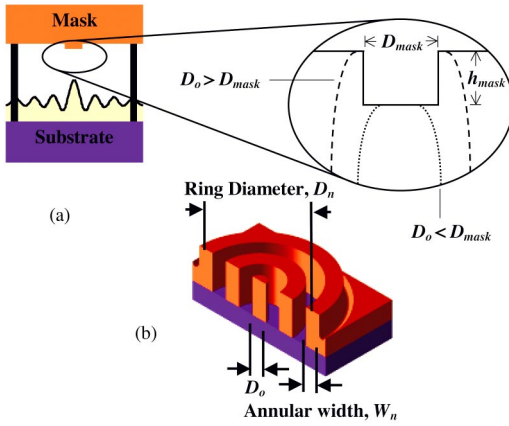
FIG. 6. (Color online) (a) The mass balance must account for the presence of a protrusion with height and diameter h_{mask} and D_{mask}. Pillars larger than the protrusion, i.e., $D_o > D_{mask}$, (dashed) are described by Eq. (25), whereas those that are smaller (dotted) are described by Eq. (24). The polymer can climb the outer edge of the mask protrusion if the diameter of the central pillar, D_o, is greater than the diameter of the mask protrusion. (b) A cut away schematic showing the ring diameter, D_n, annular width, W_n, and the diameter of the central pillar, D_o.

contrast with the pillars, though there may be some concern when the contact angles vary from 90 °.

As only one lateral length scale is relevant for the central pillar we give its diameter as

$$D_o = \frac{2LR_o^o}{\bar{k}_{max}} \sqrt{\frac{\bar{h}_o}{1 - \bar{h}_{mask}}} \quad \text{for} \quad D_o \lesssim D_{mask}, \quad (24)$$

$$D_o = \frac{2LR_o^o}{\bar{k}_{max}} \sqrt{\bar{h}_o + \bar{h}_{mask}\left(\frac{D_{mask}\bar{k}_{max}}{2LR_o^o}\right)^2}$$

$$\text{for} \quad D_o > D_{mask}, \quad (25)$$

where h_{mask} and D_{mask} are the height and diameter of the cylindrical protrusion on the mask as seen in Fig. 6. Of the two equations Eq. (24) applies when the rising column merely contacts with the lower surface of the protrusion. The latter, Eq. (25), applies when the final diameter of the pillar exceeds that of the protrusion from the mask. In this latter case the polymer climbs the sidewalls of the protrusions from the mask and may result in a lack of central pillars as in Fig. 3(b).

The results of the theory enable prediction of the cylindrically symmetric structures observed experimentally. What follows is a comparison of the theoretical results with those measured experimentally.

IV. RESULTS AND DISCUSSION

The discussion to follow critically examines the agreement between the experiment and theory. Ring diameters and annular widths follow predicted trends as a function of the ring number and mask–substrate separation. The sequential ring development is explained and the growth rates shown to

accord with theory. We conclude with a discussion on the presence of a secondary instability and emphasize the generality of the cylindrical perturbations to describe a variety of electrohydrodynamically patterned structures.

Close examination of our expressions for ring diameter and annular width, Eqs. (22) and (23), show that the ring geometry depends on several parameters, many of which were set in the course of the experiment. One parameter, the contact potential parameter, χ, must of necessity be estimated, as its value was not measured directly. This parameter represents the sum of the contact potentials at each surface and was estimated by performing a least squares fit between the measured diameters and Eq. (22) for each set of rings. We also note that our calculations assume a mask–substrate separation, H, equal to the average spacer height, 160 nm, though in reality the value of H is governed by the extent to which the spacers are forced to the bottom of the polymer film. The spacers may not have fully penetrated the polymer film during the course of the experiment (they cannot begin to penetrate until $T > T_g$).

The diameters measured from AFM scans were compared to those from the theory (see Fig. 6). As can be seen in Fig. 7 the agreement between the measurements and predictions is quite good as a function of the ring number, n, confirming the validity of the perturbation and the spacings that it implies. The approximate linearity in both the data and the corresponding theory is particularly remarkable, but not completely unexpected as spacings between Bessel function maxima quickly settle to 2π. The theory does not take the geometry of the mask protrusion or the curvature of the sidewalls into account indicating the perturbation captures most of the relevant physics. The contact potential parameters, χ (which are in fact a sum of the contact potentials at the five interfaces), range from 7.8 to 10.3 V, a range that is consistent with experimental uncertainty in determining H and other material parameters for the model.

Noting that the slopes between data points appear to be approximately constant for the diameters as a function of the ring number in Fig. 7, the ring-to-ring spacing should be approximately constant for each concentric cluster. We accordingly plot the average slope of the experimental data against the ring height as seen in Fig. 8. We had initially assumed the ring height to be an accurate measure of the mask–substrate separation, H, and as such expected the diameter to be a strongly increasing function of the same. However, the ring-to-ring spacing does not vary systematically with the measured height. Indeed, with the mask–substrate separation and the contact potential parameter as noted previously, the theory predicts a constant ring-to-ring spacing that agrees with the data. We suspect that the final ring height is determined by stretching of the rings during mask removal. The independence of the ring spacing from the measured ring height and, hence, our choice of a single value for H is reasonable, since the height is determined long after the electrohydrodynamic patterns are already fixed in the polymer film. This is not unexpected given that all of the data in Fig. 7 is from the same sample.

The data for the annular width, W_n, also follow trends expected from theory as a function of the ring number (Fig. 9). Based on the mass balance associated with Eq. (23), the
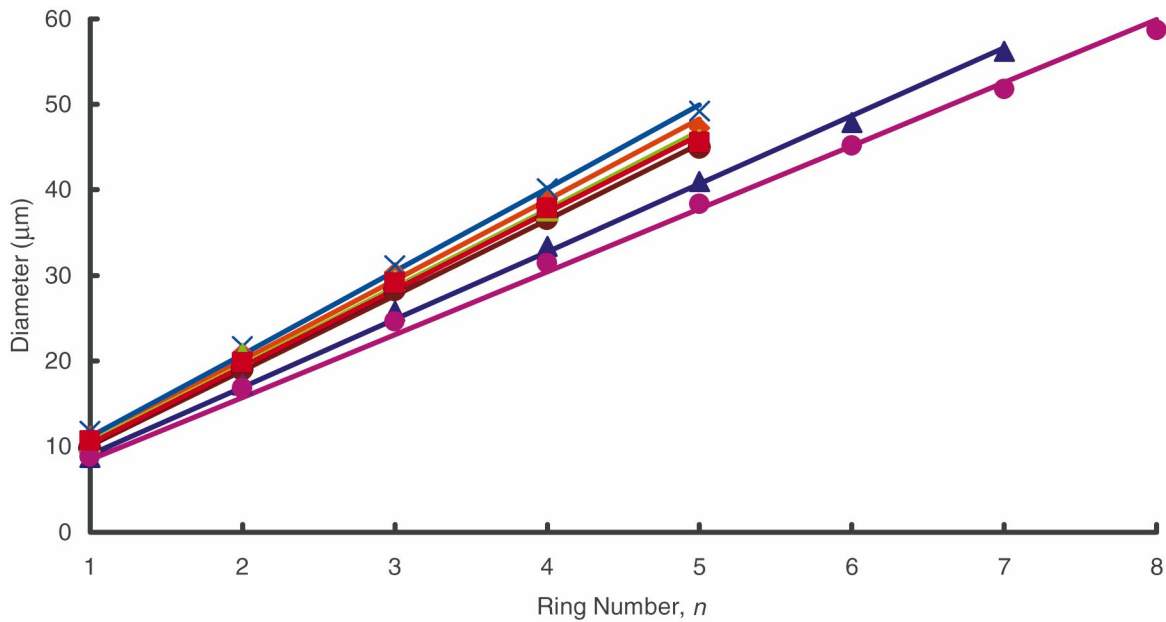
FIG. 7. (Color) The measured diameter, D_n, as a function of ring number, n, for sets of rings formed without an applied field from a 90 nm film at 90 °C with 160 nm spacer heights, 130 nm of oxide on the silicon mask, and 80 nm on the silicon substrate. The measured ring heights and estimated contact potential parameters are 202 nm and 7.8 V (royal blue ×'s), 210 nm and 10.3 V (pink circles), 234 nm and 8.1 V (orange diamonds), 257 nm and 8.3 V (green triangles), 344 nm and 8.6 V (brown circles), 414 and 9.6 V (navy blue triangles), and 648 nm and 8.4 V (red squares). The data points and theoretical fits are color coordinated for each set of concentric rings; $\varepsilon = \varepsilon^m = \varepsilon^s = 4.0$ was assumed.

theory predicts annular widths to be approximately constant for each set of concentric rings as seen in Fig. 9. The lack of dependence on the ring number, particularly beyond the first couple of rings, is seen in the data of Fig. 9. Some variation around the circumference of each ring, typically about a tenth of a micron as observed in Fig. 2, is perhaps due to local thickness variations or other localized anomalies in the field or material properties. The rings are narrower at the top and thicker at the bottom by half a micron. Accordingly, the ring widths are constant within this variation. Yet, the theory predicts annular widths in excess of those measured, the reason for which becomes clear from Fig. 10.

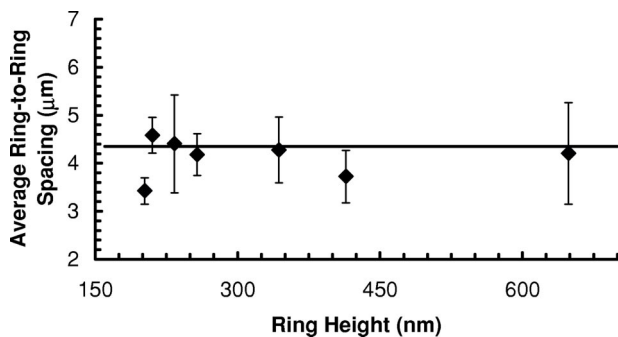Since the annular widths are approximately constant as a function of the ring number, n, we can plot the average an-

nular width as a function of the ring height (Fig. 10). The noticeable decrease in the annular widths as the ring height increases conflicts with the prediction indicated by the dashed line. The dashed line results from the mass balance described in conjunction with Eq. (23), assuming the spacing to be set by the linear stability analysis and H to be equal to the spacer height. The solid line also assumes the spacing to be set by the linear stability analysis with H as the spacer height, but that at some later time the mass is redistributed to the height measured by the AFM. One might exploit this stretching phenomenon to create thinner rings were the mechanism better understood.

Also the ratio of the diameter of the central pillar to the annular width of the first ring can be compared with theory. As seen in Fig. 9, this ratio has a mean of 1.6 ± 0.1 with no
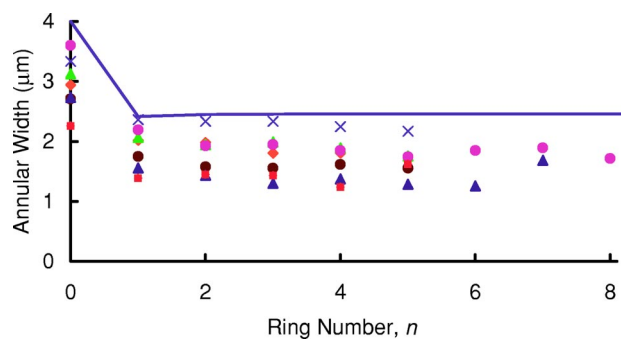

FIG. 8. The average ring-to-ring spacing ($n > 2$) as a function of the ring height for the rings described in Fig. 7. The error bars represent three standard deviations. The solid line represents the theory based on the mask–substrate separation equaling the spacer height of 160 nm. The calculations assume $\varepsilon = \varepsilon^m = \varepsilon^s = 4.0$ and a contact potential parameter of $\chi = 8.7$ V for the perfect dielectric.

FIG. 9. (Color online) The annular width, W_n, for $n > 0$ and the diameter of the central pillar, D_o, as a function of the ring number, n, for rings described in Fig. 7. The calculation (solid line) assumes the ratio of the film thickness to mask–substrate separation, h_o/H, is 0.56 and $\chi = 8.7$ V for the perfect dielectric.
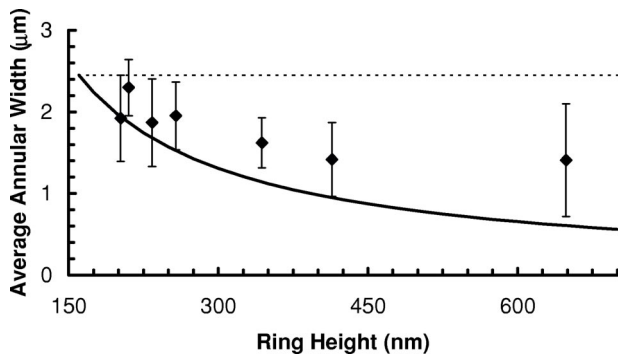
FIG. 10. The average annular width ($n>2$) as a function of the ring height for the rings described in Fig. 9. The error bars represent three standard deviations. The solid line represents the case where the initial spacing is set by the spacer height, but the rings later stretch to the measured ring height. The dashed line represents the width assuming the mask–substrate separation equals the spacer height with no adjustment. The calculations assumed $\varepsilon=\varepsilon^m=\varepsilon^s=4.0$ and $\chi=8.7$ V for the perfect dielectric.

correlation to the pillar height. Unfortunately, the length of the protrusion from the mask is not known for the rings shown in Fig. 9 as these rings were not nucleated intentionally like those in Fig. 3. By taking the ratio of Eq. (24) to Eq. (23) with $n=1$ we find that the smallest predicted value of D_o/W_I is 1.63, which occurs when $h_{mask}/H=0$, so we conclude that the protrusion for these rings was of negligible height—a reasonable result for unintended growth.

Figure 11 shows the early evolution for a set of rings observed in real time for a 90 nm film at 90 °C. The image on the left shows the pattern starting as a small pillar below the mask protrusion. After 7 min, the central pillar (dark circle) was fully formed and surrounded by a white area showing the exposed substrate and a faint halo. This halo signals the growth of a ring and is actually a region that is slightly higher than the surrounding polymer film. Note that the ring does not form from pillars or segments that later merge together. The ring is fully closed from the onset of formation. Once part of the ring has touched the mask, the contact area circles into an annulus within minutes. Subse-
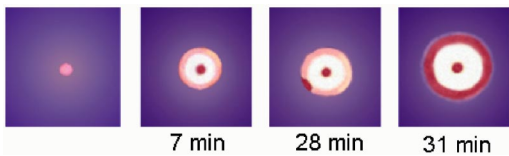

FIG. 11. (Color online) Observed kinetic formation of a 180 nm tall ring from 90 nm of film at 90 °C using a quartz mask and silicon substrate with native oxide in the absence of an applied field. The ring pattern starts from a central pillar (pink on left) whose growth is triggered by the protrusion on the mask. This initial pillar grows until it touches the mask. A bright halo (pink) and bare substrate (white) become visible seven minutes after the pillar first emerged. This halo is a ring of polymer several tens of nanometers higher than the surrounding film. Within half an hour the polymer first touches the mask and three minutes later a complete ring has formed. Subsequent rings form in the same manner as the first. The image color and contrast have been enhanced for clarity.

TABLE III. Times of formation of the nth ring as measured from the completion of the central pillar with comparison of ratios to amplitudes from the theory.

n	t_c^n (min)[a]	t_c^n/t_c^{n-1} data[b]	$J_o(R_m^{n-1})/J_o(R_m^n)$
0	0		
1	11.3	3.33	3.33
2	16.6	1.33	1.37
3	21.3	1.22	1.21

[a]Experimental conditions are similar to those in Fig. 10, but at a temperature of 105 °C. These times are from contact of the central pillar with the mask.
[b]The relative times include a 4.9 min offset, necessary for fitting $n=1$, to account for the time required to form the central pillar.

quent rings form in much the same manner as the first.

The theory can also provide some insight into the relative growth rates among a set of rings. Table III shows the time it took for a series of rings of the same concentric set to form from the moment the central pillar contacted the mask. The ratio of the times of formation of the nth and (n-1)th rings were taken and compared to the heights of the Bessel functions at R_m^n to R_m^{n-1}. The time for the formation of the central pillar (which is not exactly known) was set to 4.9 minutes to equate the measured and predicted ratios for $n=1$. The remaining ratios, corresponding to $n=2$ and 3, show good agreement, suggesting that all the rings start forming simultaneously, though they may not be macroscopically observable for several more minutes. This empirical observation suggests that the growth is linear as opposed to exponential as typically expected from linear stability analyses (see the Appendix [20]). In other words, the initial growth is approximately linear and then at some critical height the nonlinear growth takes over and contact is made shortly thereafter.

More extensive experimentation examined the temperature dependence. Figure 12 shows the variation in time be-
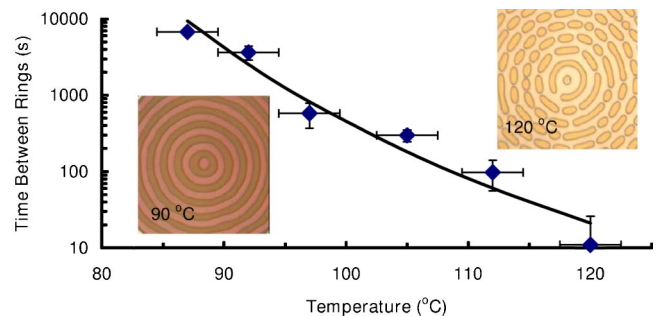

FIG. 12. (Color online) Dependence of the growth rate on temperature: the rate was quantified by measuring the time interval between the completion of the second and third rings for sets of rings formed from 90 nm of film at 90 °C using a quartz mask and silicon substrate with native oxide without an applied field. The solid line represents a fit of the WLF equation with $c_1=20.38$, $c_2=40$ °C and $T_g=75$ °C. The insets show the observed change in pattern morphology at higher temperatures due to a secondary instability.
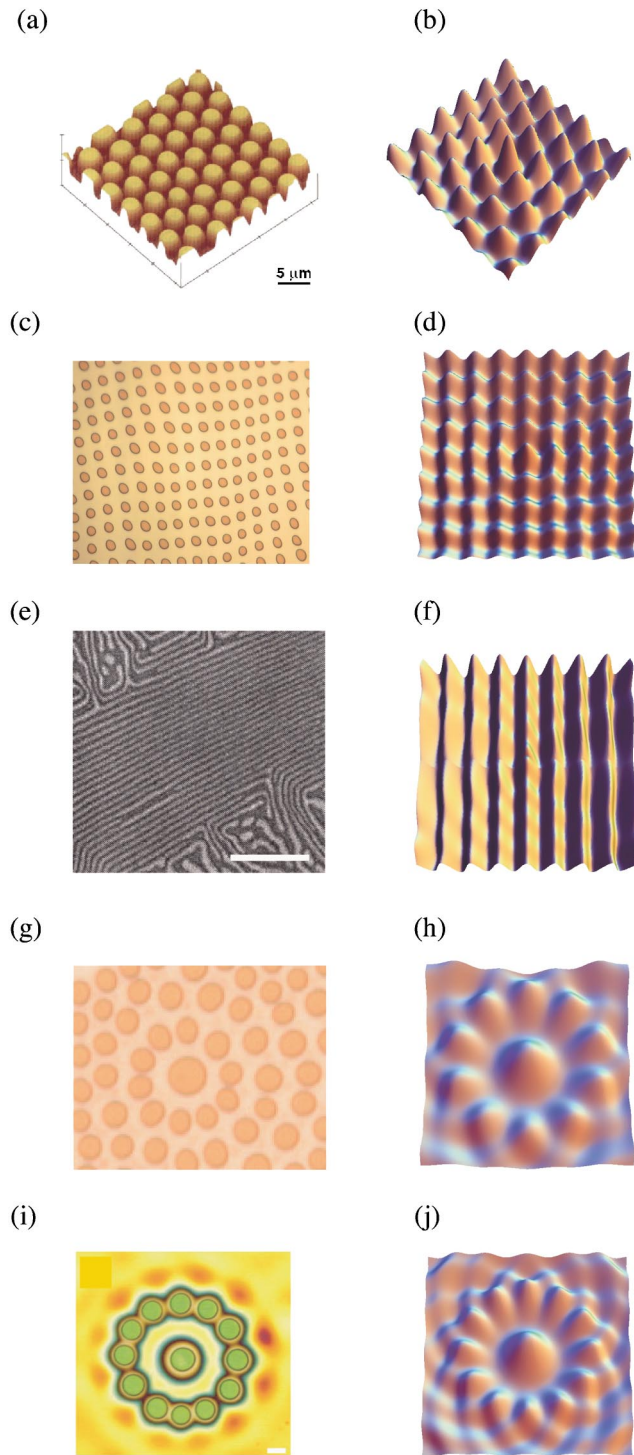
FIG. 13. (Color online) Comparison of perturbations based on sums of Bessel functions to images from the literature and experiment: hexagonal packing (a) from [6] and (b) the perturbation $\bar{h} = \bar{h}_o + \tilde{h}\Sigma_{j=0\ldots\infty}e^{i6j\theta}J_{6j}(\overline{kr})$; square packing (c) from experiments with 90 nm film at 115 °C with 160 nm spacer heights, 130 nm of oxide on the silicon mask, and native oxide on the silicon substrate without an applied field and (d) the perturbation $\bar{h} = \bar{h}_o + \tilde{h}\Sigma_{j=0\ldots\infty}e^{i4j\theta}J_{4j}(\overline{kr})$; ridges or gratings (e) from [12] and (f) the perturbation $\bar{h} = \bar{h}_o + \tilde{h}\Sigma_{j=0\ldots\infty}e^{i2j\theta}J_{2j}(\overline{kr})$; a ten pillar rosette (g) from [12] and (h) the perturbation $\bar{h} = \bar{h}_o + \tilde{h}\left[J_0\left(\frac{3}{5}\overline{kr}\right) + e^{i10\theta}J_{10}(\overline{kr})\right]$; a twelve pillar rosette (i) from [8] and (j) the perturbation $\bar{h} = \bar{h}_o + \tilde{h}\left[J_0\left(\frac{1}{2}\overline{kr}\right) + e^{i12\theta}J_{12}(\overline{kr})\right]$. The bars in (e) and (i) are 10 and 5 μm, respectively, while the widths of (c) and (g) are 40 μm and 20 μm. Panels (a), (e), (g), and (i) (www.nature.com) used with permission.

tween the formation of the second and third rings against temperature. The data shown in Fig. 12 are for sets of rings separated by at least 100 μm or more to avoid any effects of interference. The initial gap between the mask and the polymer surface was 90 nm; larger gaps seem to reduce the rate of formation commensurate with our expectations based on the theory. This temperature dependence fits with our understanding of the characteristic time for the process, $H/U = \mu\gamma H^3/(\varepsilon^g\varepsilon_o\chi^2)^2$, which is directly proportional to the viscosity, μ. The slight curvature on a semilog plot is expected,

as the viscosity of a polymer below the entanglement weight has an exponential dependence on temperature as described by Williams, Landel, and Ferry (WLF) [21,22],

$$\mu = \mu_{TG}\text{Exp}[-c_1(T - T_g)/(T - T_\infty)], \quad (26)$$

where μ_{TG} is the viscosity at the glass transition temperature, $T_\infty = T_g - c_2$ is the so called Vogel temperature, and constants c_1 and c_2 depend on polymer properties.

Complete rings form when the temperature is between the glass transition temperature and about 120 °C. Yet, for tem-

peratures of 120 °C or more, closed rings did not result as seen in the inset of Fig. 12. Instead we observed ring segments near the center and pillar arrays farther out. While our intuition initially centered on the role of higher order (i.e., $\nu > 0$) perturbations as the source of the ring segmentation, we now believe secondary instabilities to be responsible. Breaks in the rings, if only a few, are not symmetric and do not align radially, as would be expected for higher order Bessel functions. Furthermore, visual observations affirm that the divisions form after some of the film has already made contact with the mask. In consequence, we believe a later instability is responsible for breaking up the rings into discrete pillars and rings segments. Our current understanding of this secondary instability centers on a competition between surface tension and viscosity, though a thorough explanation is outside the scope of this article.

The generality of this approach, which uses Bessel functions as the basis of its perturbation, is illustrated in Fig. 13. As mentioned previously sums of Bessel functions are allowed under linear stability analyses, generating a family of possible solutions. Here we compare some members of this family to experimental images. In the left hand column are a series of images from the literature or obtained as part of these experiments. Structures range from square and hexagonal packings [6] to gratings and rosettes [8]. On the right hand side is a rendering of sums of the Bessel functions as perturbations that satisfy the linearized forms of our general equations. By an appropriate linear combination, each of the structures on the left is reproducible with remarkable fidelity. One can easily see that if the topology were set early in the process, these perturbations on the right would result in the structures on the left. Each of the perturbations utilizes sums with a single wave number except the rosettes, which require two distinct wave numbers. The pillar-to-pillar spacings of the rosettes have the same geometric ratios as those reported [8]. While direct numerical comparison for each of these structures is wanting due to the lack of quantitative experimental data, the fact that these perturbations may be constructed lends credibility to the idea that electrohydrodynamic modeling and our linear stability analysis in cylindrical coordinates may be quite general.

The hexagonal distribution of Figs. 13(a) and 13(b) merits special emphasis. Previous linear stability analyses typically assume square packing due to the nature of the exponential perturbation [see Eq. (17)]. Despite this fact, we and others have made comparison to experiments where hexagonal packing was clearly observed. Pease and Russel recently recognized that a modified Christopherson distribution captured the hexagonal packing directly [15]. Alternatively, hexagonal packing may be obtained by perturbing the film with a sum of every sixth Bessel function as

$$\bar{h} = \bar{h}_o + \tilde{h} \sum_{j=0\ldots\infty} e^{i6j\theta} J_{6j}(\bar{k}\bar{r}).$$

This construction as shown in Fig. 13(b) provides an additional route—one perhaps most relevant when local fields nucleate a central pillar followed by subsequent growth.

How the system chooses the appropriate eigenfunction is still unclear. We suspect that relief on the mask and substrate, however small, could make the selection by locally increasing the electric fields. Further modeling would be required to probe the conditions leading to the selection of the appropriate eigenfunctions as it is well known that nonlinear stability analyses are required to distinguishing among square, hexagonal and ridge packings, all of which are allowed in the linear version with the same wave number [26,27].

V. SUMMARY

In summary, we have presented sets of concentric rings obtained experimentally and developed an electrohydrodynamic description of ring and ringlike structures based on the perfect dielectric model in cylindrical coordinates. Theory developed to account for the growth of rings and cylindrical structures shows close agreement with the experimental data, predicting radial spacings, linewidths and relative growth rates. The Bessel function approach described herein is sufficiently general to describe more complicated structures found in the literature.

ACKNOWLEDGMENTS

[1] S. Y. Chou, P. R. Krauss, and P. J. Renstrom, Science **272**, 85 (1996).

[2] A. Kumar and G. M. Whitesides, Appl. Phys. Lett. **63**, 2002 (1993).

[3] C. Kim, P. E. Burrows, and S. R. Forrest, Science **288**, 831 (2000).

[4] I. I. Tarhan and G. H. Watson, Phys. Rev. Lett. **76**, 315 (1996).

[5] M. Park, C. Harrison, P. M. Chaikin, R. A. Register, and D. H. Adamson, Science **276**, 1401 (1997).

[6] S. Y. Chou and L. Zhuang, J. Vac. Sci. Technol. B **17**, 3197 (1999).

[7] S. Y. Chou, L. Zhuang, and L. J. Guo, Appl. Phys. Lett. **75**, 1004 (1999).

[8] E. Schäffer, T. Thurn-Albrecht, T. P. Russell, and U. Steiner, Nature (London) **403**, 874 (2000).

[9] X. Lei, L. Wu, P. Deshpande, Z. Yu, W. Wu, H. Ge, and S. Y. Chou, Nanotechnology **14**, 786 (2003).

[10] E. Schäffer, T. Thurn-Albrecht, T. P. Russell, and U. Steiner, Europhys. Lett. **53**, 518 (2001).

[11] Z. Q. Lin, T. Kerle, S. M. Baker, D. A. Hoagland, E. Schäffer, U. Steiner, and T. P. Russell, J. Chem. Phys. **114**, 2377 (2001).

[12] L. Zhuang, Ph.D. thesis, Princeton University, 2002.

[13] L. F. Pease III and W. B. Russel, J. Non-Newtonian Fluid Mech. **102**, 233 (2002).

[14] L. F. Pease III and W. B. Russel, J. Chem. Phys. **118**, 3790 (2003).

[15] L. F. Pease III and W. B. Russel, Langmuir **20**, 795 (2004).

[16] S. Y. Chou, MRS Bull. **26**, 512 (2001).

[17] Z. Q. Lin, T. Kerle, T. P. Russell, E. Schäffer, and U. Steiner, Macromolecules **35**, 6255 (2002).

[18] P. Deshpande, X. Y. Sun, and S. Y. Chou, Appl. Phys. Lett. **79**, 1688 (2001).

[19] D. A. Saville, Annu. Rev. Fluid Mech. **29**, 27 (1997).

[20] See EPAPS Document No. E-PLEEE8-69-067404 for details of the derivation. A direct link to this document may be found in the online article's HTML reference section. The document may also be reached via the EPAPS homepage (http:// www.aip.org/pubservs/epaps.html) or from ftp.aip.org in the directory /epaps/. See the EPAPS homepage for more information.

[21] R. G. Larson, *The Structure and Rheology of Complex Fluids* (Oxford University Press, New York, 1999).

[22] J. D. Ferry, *Viscoelastic Properties of Polymers*, 3rd ed. (Wiley, New York, 1980).

[23] G. Krizhevsky and Y. Stavsky, J. Appl. Mech. **65**, 334 (1998).

[24] B. P. Lee, J. F. Douglas, and S. C. Glotzer, Phys. Rev. E **60**, 5812 (1999).

[25] A. Karim, J. F. Douglas, G. Nisato, D. W. Liu, and E. J. Amis, Macromolecules **32**, 5917 (1999).

[26] R. Friedrichs and A. Engel, Phys. Rev. E **64**, 021406 (2001).

[27] B. Abou, J. E. Wesfreid, and S. Roux, J. Fluid Mech. **416**, 217 (2000).